Published in final edited form as:
Traffic. 2008 September ; 9(10): 1801–1810. doi:10.1111/j.1600-0854.2008.00798.x.

Intravital two-photon microscopy for studying the uptake and trafficking of fluorescently conjugated molecules in live rodents

Andrius Masedunskas[1,2] and **Roberto Weigert**[1,*]

[1]Intracellular Membrane Trafficking Unit,Oral and Pharyngeal Cancer Branch National Institute of Dental and Craniofacial Research, National Institute of Health 30 Convent Dr. 303A, Bethesda, MD 20892-4340

[2]Department of Biology – University of North Carolina at Chapel Hill

Abstract

Here we describe an experimental system based on intravital two-photon microscopy for studying endocytosis in live animals. The rodent submandibular glands were chosen as model organs since they can be exposed easily, imaged without compromising their function and, furthermore, they are amenable to pharmacological and genetic manipulations. We show that the fibroblasts within the stroma of the glands readily internalize systemically injected molecules such as fluorescently conjugated dextran and bovine serum albumin, providing a robust model to study endocytosis. We dynamically image the trafficking of these probes from the early endosomes to the late endosomes and lysosomes while also visualizing homotypic fusion events between early endosomes. Finally, we demonstrate that pharmacological agents can be delivered specifically to the submandibular salivary glands thus providing a powerful tool to study the molecular machinery regulating endocytosis in a physiological context.

Keywords

Intravital microscopy; Two-photon microscopy; Endocytosis; Membrane Traffic; Salivary Glands

Introduction

Endocytosis is a key process necessary for a variety of cellular events such as nutrient uptake, cell signaling, cell polarity, remodeling of the plasma membrane, neurotransmission, immunity, and is also exploited by various pathogens as portal of entry into the target cells (1). So far, endocytic pathways have been studied and characterized by using cell cultures grown on two-dimensional surfaces (2–4). Although this experimental system has provided key information about the endocytic machinery, it lacks two essential components that are characteristic of cells in their native tissue: the three-dimensional architecture and the interactions with other cells. As a consequence, many fundamental questions about the machinery regulating endocytosis are still unanswered. To address these questions, an experimental system aimed at studying endocytosis in a physiological context, namely in live animals, has to be set up.

To this aim, non-linear optical imaging techniques such as intravital two-photon microscopy (TPM), which allows imaging thick tissues, in situ, at a sub-cellular resolution, could be used (5,6). To gain additional information on the tissue architecture, TPM could be complemented

*To whom the correspondence should be addressed: E-mail: weigertr@mail.nih.gov.

with another technique, such as second harmonic generation (SHG), which allows imaging molecules such as collagen when organized in fibrils (7,8). One of the major advantages of these techniques is that specimens are excited with near infra-red (NIR) light, which has a deeper tissue penetration than visible or UV light and under the appropriate conditions does not induce significant photodamage to the tissues (5,6,9). Furthermore, various endogenous molecules can be excited by either TPM or SHG (8,10) and due to their broad two-photon excitation spectra, multiple fluorophores can be excited at the same time using a single wavelength (10,11). Recently, TPM has been used to visualize in living animals different intact tissues such as lymphatic organs, skin, heart and brain (12–14), and to visualize the endocytosis of the folate receptor and other fluorescent probes in the kidney (15,16). Although sub-cellular organelles such as endosomes and lipid droplets have been imaged dynamically by using either TPM or third harmonic generation (15,17), long term imaging and tracking of such structures has yet to be achieved.

As an experimental model system, the submandibular salivary glands (SSGs) of live rodents offer various advantages. The glands can be easily exposed by a minor surgical procedure and they can be manipulated both pharmacologically and genetically. Indeed, pharmacological agents, and naked DNA or viral particles harboring genes of interest, can be specifically targeted to the glands by retro-injection into the major excretory duct (Wharton's duct) (18–20).

In this study we show that the internalization and trafficking of systemically injected fluorescently conjugated probes, such as dextran or bovine serum albumin (BSA), can be imaged dynamically in the SSGs of live rodents by using TPM. These probes are rapidly internalized into early endosomes of fibroblasts within 20–30 minutes after the injection. The early endosomes undergo homotypic fusion in the periphery of the cells, and after 30–40 minutes, reach late endosomal/lysosomal structures in the perinuclear area. Furthermore, we show that drugs known to affect the actin cytoskeleton, such as latrunculin A (LatA) and cytochalasin D (CytD), can be effectively delivered in the SSGs by injections through the Wharton's ducts, providing an exceptional tool to manipulate the endocytic processes in vivo. In summary, we show that a combination of non-linear imaging techniques and a pharmacological approach can be successfully used to study dynamically the molecular machinery that regulates endocytosis and membrane traffic in live animals.

Results

Three-dimensional and dynamic imaging of the rat submandibular salivary glands by intra-vital TPM

As an experimental model to study endocytosis we used the SSGs of living rats. The parenchyma of these exocrine glands is mainly composed by acini and a complex system of ducts. As shown in Figure 1A, these structures are formed by polarized epithelial cells with the apical domain facing either the acinar canaliculi or the lumen of the ducts, and the basolateral domain facing the stroma (21, 22). Other supporting cells are present in the parenchyma, such as myoepithelial cells and fibroblasts, which surround the acini and are dispersed in the stroma (Figure 1A) (21, 23). First, we determined whether we could image the architecture of isolated rat SSGs using TPM. To visualize the morphology of the cells we took advantage of the fluorescence that various endogenous molecules emit by non-linear excitation in the NIR range (8, 10). The optimal imaging conditions were determined by exciting the same area of the gland, using various wavelengths between 690 nm and 990 nm, and collecting the emitted light below 510 nm (see Materials and Methods). The brightest signal outlining the shape of the cells was generated exciting between 730 nm and 750 nm (Figure S1). Signals outlining large elastic fibers were detected exciting between 800 nm and 960 nm, most likely representing a combination of two-photon and second harmonic signals (Figure S1). We

acquired sequential images along the Z-axis from the surface of the gland up to 70–100 μm into the tissue. The very same volume was imaged exciting first at 750 nm to image the parenchyma (Figure 1B, 2 and 3 grey) and then at 900 nm to image the elastic fibers (Figure1B, 1, green and movie S1 and S2). The optical sections were combined (Figure 1B, 1–3) and a 3D reconstruction was generated (Figure 1B, lower panel). Due to their distinct morphology, the acini and the ducts were easily identified (Figure 1B, arrows and arrowhead respectively). Furthermore, some structural features such as the acinar canaliculi or the mitochondrial-enriched basolateral pole of the striated ducts were also captured (Figure 1B insets). The 3D reconstruction shows, as expected, that the acinar and the ductal cells lay beneath the layers of elastic fibers that occupied the uppermost 10–15 μm of the gland (Figure 1B, lower panel). A similar architecture was observed in the mice SSGs (not shown).

Next, we determined whether we could dynamically image the parenchyma of the SSGs and visualize the vasculature in the live animal. To this aim a catheter was inserted in the tail artery of a rat, and the glands were exposed by an incision in the submandibular area. One of the glands, while still connected to the vasculature and the central nervous system, was externalized and placed onto a custom-made holder (Figure 1C). In order to minimize the motion due to the respiration and the heartbeat, the holder was slightly elevated and detached from the body of the animal (Figure 1C). The animal was then moved to an adjustable stage adjacent to the microscope, and a water-immersion lens was brought on top of the gland by using an objective inverter (13) (Figure 1C). A carbomer-based optical coupling gel was applied to image the gland and to prevent the dehydration of the tissue (13). The temperature of the gland was monitored by a probe and adjusted by the objective temperature control at 38±1°C, a range matching the physiological temperature reported for the rats (24). Under these conditions the gland was still functional as established by measuring the agonist-stimulated secretion of saliva (not shown). The SSGs were imaged in time-lapse exciting at 750 nm and although some rhythmic movement of the gland was observed, the overall motion did not affect the acquisition quality of the images (movie S3). Notably, the average power of the laser measured at the objective was maintained below 5 mW to prevent any photodamage. To highlight the vasculature, 500 kDa FITC-dextran (FITC-D) was injected into the tail artery. Almost instantly, the dextran filled the vasculature where it was retained for the entire duration of the experiment (Figure1D and movie S3). The same experiment was performed highlighting the nuclei by injecting Hoechst 33342 prior to the injection of 500 kDa FITC-D (Figure 1E and movie S4). These data show that the parenchyma and the vasculature of the exposed SSGs could be imaged dynamically in live rats. Furthermore, the procedures we have developed substantially reduce the motion due to the respiration and the heartbeat that is one of the major obstacles to intravital studies.

Internalization of systemically injected fluorescently labeled dextran in living rodents

Next, we imaged the endocytosis of fluorescently labeled molecules in the SSGs. Similar to what is used for cultured cells, we used fluorescently-labeled dextrans to follow fluid phase constitutive endocytosis (25). We chose a 70 kDa dextran since it diffuses out from the vasculature in the SSGs and is retained in the circulation for a longer period of time when compared to dextrans of smaller sizes (not shown). Seventy kDa Texas Red Dextran (TXR-D) was injected into the tail artery and after 1 hr the SSGs were imaged by TPM. A Z-stack of images revealed that two distinct populations of cells internalized dextran: one that is embedded within the elastic fibers (Figure 2A–1) and the other that is located in the stroma around both acinar and ductal structures (Figure 2A–2 and Figure 2B arrow and arrowhead). As shown in Figure 2C, both populations of cells were positive for vimentin suggesting that they are fibroblastic in nature. Notably, dextran was not detected in either acini or ducts even after longer period of times from the injection or upon administration of higher doses of the probe (Figure 2C and not shown). Internalized dextran was observed in vesicular structures of

different sizes that were localized both in the periphery of the cells or around the nuclei (Figure 2D). A similar pattern was observed either injecting TXR-D in mice or injecting another probe such as TXR-BSA (Figure S2). Next, we dynamically imaged the internalization of the dextran in the SSGs of live animals. Since the distribution and the type of cells that internalize dextran was homogeneous throughout the entire gland (not shown) we chose to image within the first 10–30 μm below the surface. Hoechst was injected systemically and the SSGs were exposed and imaged (Fig. 2E, left panel, time 0:00). After 2 min and 30 sec, TXR-D was injected into the tail artery and almost immediately it appeared in the vasculature of the gland (movie S5). Four to 5 minutes after injection, small fluorescent round structures appeared in some of the cells close to a blood vessel (Figure 2E, time 7:00, arrowheads). From 5–20 minutes they increased both in number and in size (Figure 2E, time -15:00 and time - 20:00, arrows and movie S5). From 30 minutes to 1 hr, the number of dextran-containing structures did not change significantly while they accumulated in the perinuclear area (see below and movie S6). Notably, the distribution of the vesicular structures, the number and the type of cells that internalized dextran were not affected by either the externalization of the SSGs or the injection of Hoechst (not shown).

To determine the kinetics of the trafficking through the various endocytic compartments, we first injected the rats with TXR-D to load the lysosomal compartment and after 24 hours we injected 70 kDa Alexa 488 dextran (488-D) to image the early endosomal compartments. The glands were removed at different times after the injections of 488-D and imaged as described above. As expected, TXR-D accumulated in lysosomal structures labeled by the late endosomal/lysosomal marker LAMP-1 (26) (Figure 3A). After 20 minutes from the second injection, 488-D was present in early endosomes. This was determined by two line of evidences: first, 488-D containing endosomes did not overlap with the late endosomes/ lysosomes containing TXR-D (Figure 3B, top panel) and second, the 488-D containing endosomes were not labeled by LAMP-1 (not shown). After 30 minutes (Figure 3B, lower panel, arrowheads) a significant overlap was observed and after 60 minutes most of the 488-D dextran reached the late endosomal/lysosomal compartment (not shown). Notably, the progression of the cargoes from the early endosomes to the late endosomes/lysosomes is consistent with that reported for cultured cells (27). To image the fusion events between the various endosomal compartments dynamically we set up a time-lapse acquisition upon the second injection of 488-D. After 5 minutes from the injection, the 488-D appeared in small peripheral early endosomes (Figure 3C - time 7:00), which did not reach the lysosomal compartment but increased in size in the first 20–25 minutes. (Figure 3C - time 15:00 and 25:00, and movie S6). The size of the endosomes increased due to homotypic fusion events as shown in Figure 3D where two small early endosomes came in contact and fused, generating a larger endosome which did not contain any TXR (Figure 3D, arrowheads and movie S7). These fusion events are not always obvious since they occur within 3 seconds, a time that is very close to the time interval between each frame of the time-lapse sequence. At later time point we detected fusion events between larger endosomes containing only 488-D. These structures most likely represent late endosomes since they overlapped with LAMP-1 (not shown). Notably, we did not observe any direct fusion events between endosomes containing 488-D and lysosomes containing TXR-D. Instead, the 488-D containing endosomes gradually acquired TXR-D (Figure 3E, time - 55:00 vs. time 56:38, insets and arrowheads), and then fused with another endosome containing both 488-D and TXR-D (Figure 3E, time 57:57 and 58:14, inset and arrow, and movie S8). Due to the limit in the resolution of TPM we could not determine the mechanisms by which the 488-D acquired the TXR-D, which most likely implicates some transient connections as previously described by Luzio and colleagues (27).

Delivery of drugs to the rat submandibular salivary glands by injections through the Wharton's duct

We have shown that the trafficking of probes through early endosomes and late endosomes/lysosomes can be studied in live animals. However, an important pre-requisite to study the molecular machinery regulating these processes is the ability to perturb this system. In this regard, the Wharton's duct provides a direct route to deliver drugs into the submandibular glands. This avoids systemic injections, which might lead to broader non-specific effects to the entire animal. To check how effectively molecules can be delivered throughout the SSGs, a fine polyethylene cannula was inserted into the Wharton's duct (see Figure 4A). The 488-D was injected through the cannula. Almost immediately, it appeared in large circular structures that most likely represent the cross sections of the terminal blunt end portion of large ducts (Figure 4, B and C, arrow and diagram in Figure 1A). Immediately after, 488-D appeared in small ducts and in the acinar canaliculi (Figure 4B and 4C, arrowheads and movie S9), which as expected, did not overlap with the vasculature as shown by TXR-D labeling of the blood volume (Figure 4C). In order to test whether drugs delivered through this route would exert their effect throughout the entire gland we injected LatA or CytD, two molecules known to disrupt the actin cytoskeleton. A rat was first systemically injected with TXR-D to label the endosomal and the lysosomal compartments. After one hour, one gland was injected with LatA or CytD, while the other gland was injected with the vehicle, and 45 minutes later, 488-D was injected systemically. The glands were excised and imaged after one hour. CytD (Figure 4, D and E, and LatA not shown) was indeed effective in disrupting the filamentous actin cytoskeleton in many areas of the glands as shown by cryo-sections, while other organs were not affected (not shown). Notably, both drugs reduced the internalization of 488-D when compared with control glands while the levels of TXR-D injected prior to the drugs were not affected (LatA, Figure 4, F and G and CytD not shown). How these drugs affected the fluid phase endocytosis in the gland remains to be investigated, but the results serve as a proof of principle that drugs can be selectively and effectively delivered to the SSGs without affecting other organs.

Discussion

Endocytosis and membrane traffic have been studied primarily in two dimensional cell culture systems, an experimental model system that offers many advantages. For example, cells in culture can be easily manipulated by gene expression, gene ablation, or pharmacological tools. Furthermore, in the last few years the use of time-lapse confocal microscopy has allowed to collect an enormous body of information about the dynamics and the molecular machinery involved in many intracellular events. Nonetheless, the major drawbacks of cultured cells is that their spatial organization is very different from that of cells growing in a living tissue where they have a three-dimensional organization and most importantly, they interact with other cells both directly, via physical interactions, and indirectly, via signaling molecules. Thus, studying cell behavior in the live animal could lead to new important discoveries. Along this line some pioneering studies were carried out by Ann Hubbard and colleagues (28) who investigated the internalization of EGF by hepatocytes in the perfused rat liver. These studies, that were based on electron microscopy, provided very detailed insight on the ultrastructure of the endosomal system and the trafficking of the EGF through the endosomal compartments. However, a major limitation of this approach was the lack of information on the dynamic of the endocytic processes.

To this aim we set up an experimental system, which enables to dynamically image the uptake and trafficking of fluorescent molecules in live rodents.

Here we show that the combination of intravital TPM as imaging technique, and the rodent SSGs as model organ, offers many advantages to study endocytosis in live animals. The first

advantage is that TPM allows to visualize at the same time the parenchyma of the tissue, the extracellular matrix, and a broad spectrum of fluorescent probes that are administered exogenously. This is possible since the two-photon excitation spectra of many fluorophores, including endogenous molecules and elastic fibers are broad and thus they can be excited using a single wavelength (10,11). Indeed, we show that the structures of the acini and the ducts can be easily resolved by performing three-dimensional reconstructions and furthermore, that the structure and the dynamics of both the vasculature and the salivary ducts can also be imaged. Further studies on the nature and the characteristics of these endogenous signals needs to be pursued in the near future and extended to other tissues. A second advantage of using TPM is that below certain doses the IR light does not induce any major radiation damage, thereby allowing to extend time-lapse experiments for longer periods of time. Notably, we were able to track small endosomal structures imaging fusion events for over 20 minutes. Furthermore, using different combinations of fluorescent dextrans and distinct times of injections we were also able to visualize the progression of the endosomal structures towards the late endosomes/lysosomes. However, TPM showed some limitations due to its reduced sensitivity. For example, smaller structures during the first step of internalization could not be detected.

The first advantage of choosing the SSGs as a model organ is that they are accessible, and thus they can be easily exposed and externalized without compromising their functions. Furthermore, SSGs can be accommodated into a custom-made holder that has been designed to minimize the motion due to the heartbeat and the respiration of the live animal, which is one of the major obstacles to intravital imaging. Under these conditions, the glands still receive the nutrients through the vasculature and are able to undergo stimulated secretion and fluid-phase endocytosis. Notably, we found that fibroblasts in the parenchyma of the glands, but not acinar or ductal cells, are able to internalize fluid-phase markers such as dextrans, indicating that distinct cell populations within the same tissue behave differently. Although here we focus on the trafficking of fluid-phase markers, this approach can be extended to other forms of endocytosis, such as the receptor-mediated pathways, that might be more prominent in the acinar cells, where they might play an essential role in the down regulation of G-protein-coupled receptors or in the transcytosis of IgA (29,30). Furthermore, we showed that the SSGs can be specifically manipulated pharmacologically without affecting other organs by injecting molecules through the Wharton's duct. As a proof of principle, we have shown that drugs such as LatA and CytD, which disrupt the actin cytoskeleton, can exert their effect on the entire SSGs, thus providing a powerful tool to study the molecular machinery regulating endocytosis. We are currently exploring the possibility to transduce genes into the salivary glands to label intracellular compartments, as well as to express molecules acting as dominant negative mutants and to deliver shRNAs, thus providing powerful molecular tools to study the membrane trafficking process *in vivo*. Finally, the use of genetically engineered mouse models will add another valuable tool to carry out studies in live animals.

Although we chose to use the SSGs as model organs other tissues can be successfully used as shown in the case of the kidneys (15). The major challenges will be to develop surgical techniques to expose the organ of interest with the minimal damage, to develop special tools to minimize the motion transferred from the animal, and finally, to develop the appropriate methodology for specific delivery of genes or molecules to the target cells within the tissues of interest.

Material and Methods

Two-photon microscopy and imaging

An IX81 inverted confocal microscope (Olympus, Melville, NY) was modified to perform two-photon microscopy. A tunable Ti:Sapphire femtosecond laser, Chameleon Ultra II (Coherent, Santa Clara, CA) was used as laser source and the power was modulated using a

combination of neutral density filters (Chroma Technologies, Rockingham, VT). The size of the beam was modulated using a beam expander (LSM Technology Inc., Shrewsbury, PA) and directed into a Fluoview 1000 scanning head (Olympus, Melville, NY). The emitted signal was directed into a custom-made array of three non-descanned detectors that were installed on the right port of the microscope (LSM Technology Inc., Shrewsbury, PA). A 680 nm barrier filter (Chroma Technologies, Rockingham, VT) was used to prevent the scattered IR light to reach the detectors. The three cooled PMTs were purchased from Hamamtzu (R6060-12), the two dichroic mirrors and the barrier filters were purchased from Chroma Technologies. Hoechst, the endogenous fluorescence and the SH signal were detected on the first PMT (dichroic mirror 510 nm, barrier filter 400 nm-480 nm). FITC and Alexa 488 were detected on the second PMT (dichroic mirror 570 nm, barrier filter 505 nm-560 nm) and Texas Red on the third PMT (barrier filter 590 nm-650 nm). To enhance the detection of the endogenous fluorescence the barrier filter was removed. The excised glands were imaged in the inverted setting while time lapse imaging on the live animal was performed in the upright configuration using an objective inverter (LSM Technology Inc., Shrewsbury, PA) (13). For the time lapse imaging the acquisition speed was set to 0.3 frames/sec. All the images and movies were acquired using a UPLSAPO 60X NA 1.2 water immersion objective with the exception of supplementary Figure1, Figure 4B, Figure 4C and supplementary movie 9) that were acquired using a XLUMPFL20XW 20X NA 0.95 water immersion objective (Olympus, Melville, NY). All images were acquired in two-photon modality with the exception of Figure 2C, 3A, 4D and E that were acquired using the IX81 in confocal modality.

Animal Preparation

All the experiments were approved by the National Institute of Dental and Craniofacial Research (NIDCR, National Institute of Health, Bethesda, MD) Animal Care and Use Committee. Sprague-Dawley male rats weighing from 150–250 g and FVB mice weighing 30–50 g were fed ad libitum. The animals were anesthetized by an IM injection of a mixture of Ketamine and Xylazine (100 mg/Kg an 20 mg/Kg respectively) with additional injections as needed. For the systemic injections, the tail artery was surgically exposed, and a small incision was performed to insert a fine catheter connected to a 1 ml syringe. The tail was sutured and small amounts of saline (100–200 µl) were injected as needed. Unless otherwise specified the rats were injected with the following amount of fluorescent probes: 200 µg 70 kDa TXR-D, 200 µg 70 kDa 488-D, 40 µg 500 kDa FITC-D and 10 µg of Hoechst 33342 (Invitrogen, Carlsbad, CA). To image the isolated SSGs, the rats were euthanized by carbon dioxide, the glands were excised and placed either in PBS or fixed in 4% formaldehyde for 1 hr and stored in PBS at 4°C. For injections into the Wharton's duct a fine polyethylene cannula (PE5 or PE8) was inserted in the orifice below the tongue using tweezers. The cannulae were inserted for 0.2–0.5 cm and sealed with either glue or low melting agarose. The volume injected did not exceed 75–100 µl and the injections were performed very slowly to prevent any damage to the glands. All the fluorescent probes were purchased from Invitrogen (Carlsbad, CA) and diluted in sterile saline at the appropriate concentrations (see figure legends) in a volume not exceeding 200 µl. To couple the sample to the objective a carbomer-940 based gel (Snowdrift farm, Tucson, AZ) was prepared and used as described previously (13). The temperature of the externalized glands was maintained using the objective heater (Bioptechs, Butler, PA) and the temperature of the body was maintained by a water-circulating heated pad (Kent scientific, Torrington, CT).

Image processing

When needed, the background noise was reduced by applying to each image one or two rounds of a 2×2 pixel low-pass filter by using Metamorph (Molecular Devices, Sunnyvale, CA). Brightness, contrast and gamma correction were applied with the exception of Figure 4F and G. For supplementary movie 4 and 9, adjustments in the alignment of the frames were

performed using ImageJ (W. Rasband, National Institute of Health, Bethesda, MD) plug-in Stackreg (31). Volume rendering was performed using Imaris 5.6 and 6.0 64 bit (Bitplane, Saint Paul, MN). The final preparation of the images was conducted with Adobe Photoshop CS. Movies were assembled with Metamorph and compressed with Quicktime Pro.

Whole mount immuno-cytochemistry

Isolated glands were fixed for 20 minutes in 0.05% Glutharaldehyde/4% formaldehyde in 0.2M Hepes pH 7.3 and then transferred for 1 hr in 4% formaldehyde. The glands were sliced from the surface and fixed again in 4% formaldehyde for 30 minutes. The fixative was washed in PBS and the slices were blocked O.N. at 4°C in PBS, 10% fetal bovine serum, 0.04% saponin (blocking solution). The slices were incubated for 1 hour with the primary antibody in blocking solution, washed 3 × 10' in PBS and then incubated with the appropriate secondary antibody for 1 hour at R.T.. The samples were washed 3 × 10' in PBS and then imaged by either two-photon or confocal microscopy. The primary antibodies used in this study were the following: rabbit anti-vimentin (Dako, Carpinteria, CA), rabbit anti Lamp-1 (Abcam, Cambridge, MA). As secondary antibody we used Alexa 488-goat anti-rabbit IgG (Invitrogen, Carlsbad, CA).

Cryo-sections

OCT-embedded frozen tissues were cut (15 μm) onto silanated glass slides and fixed for 1 hr in 2% formaldehyde. Cryo-sections were incubated with blocking solution for 1h and immuno-stained as described above. To label the actin cytoskeleton, Alexa 488-phalloidin (Invitrogen, Carlsbad, CA) was used.

Supplementary Material

Refer to Web version on PubMed Central for supplementary material.

Abbreviations

(SSGs), Submandibular salivary glands; (TPM), Two-photon microscopy; (TXR-D), Texas-Red Dextran; (488-D), Alexa 488 Dextran; (LatA), Latrunculin A; (CytD), Cytochalasin D.

Acknowledgements

We thank Drs. Julie Donaldson, Silvio Gutkind and Jennifer Lippincott-Schwartz for the critical reading of the manuscript, Dr. Alfredo Molinolo (OPCB), and the other members of the IMTU for their invaluable assistance. A.M. is part of the UNC-NIH Graduate Program Partnership in Cell Motility and the Cytoskeleton

References

1. Mellman I. Endocytosis and molecular sorting. Annu Rev Cell Dev Biol 1996;12:575–625. [PubMed: 8970738]
2. Conner SD, Schmid SL. Regulated portals of entry into the cell. Nature 2003;422(6927):37–44. [PubMed: 12621426]
3. Maxfield FR, McGraw TE. Endocytic recycling. Nature reviews 2004;5(2):121–132.
4. Mayor S, Pagano RE. Pathways of clathrin-independent endocytosis. Nature reviews 2007;8(8):603–612.
5. Helmchen F, Denk W. Deep tissue two-photon microscopy. Nat Methods 2005;2(12):932–940. [PubMed: 16299478]
6. Zipfel WR, Williams RM, Webb WW. Nonlinear magic: multiphoton microscopy in the biosciences. Nat Biotechnol 2003;21(11):1369–1377. [PubMed: 14595365]
7. Campagnola PJ, Loew LM. Second-harmonic imaging microscopy for visualizing biomolecular arrays in cells, tissues and organisms. Nat Biotechnol 2003;21(11):1356–1360. [PubMed: 14595363]

8. Zipfel WR, Williams RM, Christie R, Nikitin AY, Hyman BT, Webb WW. Live tissue intrinsic emission microscopy using multiphoton-excited native fluorescence and second harmonic generation. Proc Natl Acad Sci U S A 2003;100(12):7075–7080. [PubMed: 12756303]
9. Diaspro A, Shepard CJR. Two-Photon Microscopy: Basic Principles and Architectures. 2002
10. Hsu L, Kim KH, Dong C, Kaplan P, Hancewics T, Buehler C, Berland KM, Masters BR, So PTC. Two-Photon Imaging of Tissue Physiology Based on Endogenous Fluorophore. 2002
11. Xu C. Cross-Sections of Fluorescent molecules in Confocal and Two-Photon Microscopy. 2002
12. Qi H, Egen JG, Huang AY, Germain RN. Extrafollicular activation of lymph node B cells by antigen-bearing dendritic cells. Science 2006;312(5780):1672–1676. [PubMed: 16778060]
13. Rothstein EC, Nauman M, Chesnick S, Balaban RS. Multi-photon excitation microscopy in intact animals. J Microsc 2006;222(Pt 1):58–64. [PubMed: 16734715]
14. Svoboda K, Yasuda R. Principles of two-photon excitation microscopy and its applications to neuroscience. Neuron 2006;50(6):823–839. [PubMed: 16772166]
15. Sandoval RM, Kennedy MD, Low PS, Molitoris BA. Uptake and trafficking of fluorescent conjugates of folic acid in intact kidney determined using intravital two-photon microscopy. Am J Physiol Cell Physiol 2004;287(2):C517–C526. [PubMed: 15102609]
16. Dunn KW, Sandoval RM, Kelly KJ, Dagher PC, Tanner GA, Atkinson SJ, Bacallao RL, Molitoris BA. Functional studies of the kidney of living animals using multicolor two-photon microscopy. Am J Physiol Cell Physiol 2002;283(3):C905–C916. [PubMed: 12176747]
17. Debarre D, Supatto W, Pena AM, Fabre A, Tordjmann T, Combettes L, Schanne-Klein MC, Beaurepaire E. Imaging lipid bodies in cells and tissues using third-harmonic generation microscopy. Nat Methods 2006;3(1):47–53. [PubMed: 16369553]
18. Goldfine ID, German MS, Tseng HC, Wang J, Bolaffi JL, Chen JW, Olson DC, Rothman SS. The endocrine secretion of human insulin and growth hormone by exocrine glands of the gastrointestinal tract. Nat Biotechnol 1997;15(13):1378–1382. [PubMed: 9415890]
19. Oliver C, Hand AR. Uptake and fate of luminally administered horseradish peroxidase in resting and isoproterenol-stimulated rat parotid acinar cells. J Cell Biol 1978;76(1):207–229. [PubMed: 618893]
20. Voutetakis A, Bossis I, Kok MR, Zhang W, Wang J, Cotrim AP, Zheng C, Chiorini JA, Nieman LK, Baum BJ. Salivary glands as a potential gene transfer target for gene therapeutics of some monogenetic endocrine disorders. J Endocrinol 2005;185(3):363–372. [PubMed: 15930162]
21. Sato A, Miyoshi S. Ultrastructure of the main excretory duct epithelia of the rat parotid and submandibular glands with a review of the literature. Anat Rec 1988;220(3):239–251. [PubMed: 3284416]
22. Watanabe I, Seguchi H, Okada T, Kobayashi T, Jin QS, Jiang XD. Fine structure of the acinar and duct cell components in the parotid and submandibular salivary glands of the rat: a TEM, SEM, and HRSEM study. Histol Histopathol 1996;11(1):103–110. [PubMed: 8720453]
23. Ogawa Y. Immunocytochemistry of myoepithelial cells in the salivary glands. Prog Histochem Cytochem 2003;38(4):343–426. [PubMed: 14509196]
24. Cammack DES KM, Eichen PA, Lamberson WR. Relationships between body temperature and performance traits in heatstressed rats. Journal of Thermal Biology 2005;30(6):467–477.Corresponding Author Contact Information.
25. Racoosin EL, Swanson JA. Macropinosome maturation and fusion with tubular lysosomes in macrophages. J Cell Biol 1993;121(5):1011–1020. [PubMed: 8099075]
26. Rohrer J, Schweizer A, Russell D, Kornfeld S. The targeting of Lamp1 to lysosomes is dependent on the spacing of its cytoplasmic tail tyrosine sorting motif relative to the membrane. J Cell Biol 1996;132(4):565–576. [PubMed: 8647888]
27. Bright NA, Gratian MJ, Luzio JP. Endocytic delivery to lysosomes mediated by concurrent fusion and kissing events in living cells. Curr Biol 2005;15(4):360–365. [PubMed: 15723798]
28. Dunn WA, Hubbard AL. Receptor-mediated endocytosis of epidermal growth factor by hepatocytes in the perfused rat liver: ligand and receptor dynamics. J Cell Biol 1984;98(6):2148–2159. [PubMed: 6327725]
29. Hu Y, Purushotham KR, Wang P, Dawson R Jr, Humphreys-Beher MG. Downregulation of beta-adrenergic receptors and signal transduction response in salivary glands of NOD mice. Am J Physiol 1994;266(3 Pt 1):G433–G443. [PubMed: 8166282]

30. Proctor GB, Carpenter GH, Segawa A, Garrett JR, Ebersole L. Constitutive secretion of immunoglobulin A and other proteins into lumina of unstimulated submandibular glands in anaesthetised rats. Exp Physiol 2003;88(1):7–12. [PubMed: 12525850]

31. Thevenaz PR, UE Unser M. A pyramid approach to subpixel registration based on intensity. Image Processing, IEEE Transactions 1998;7(1):27–41.

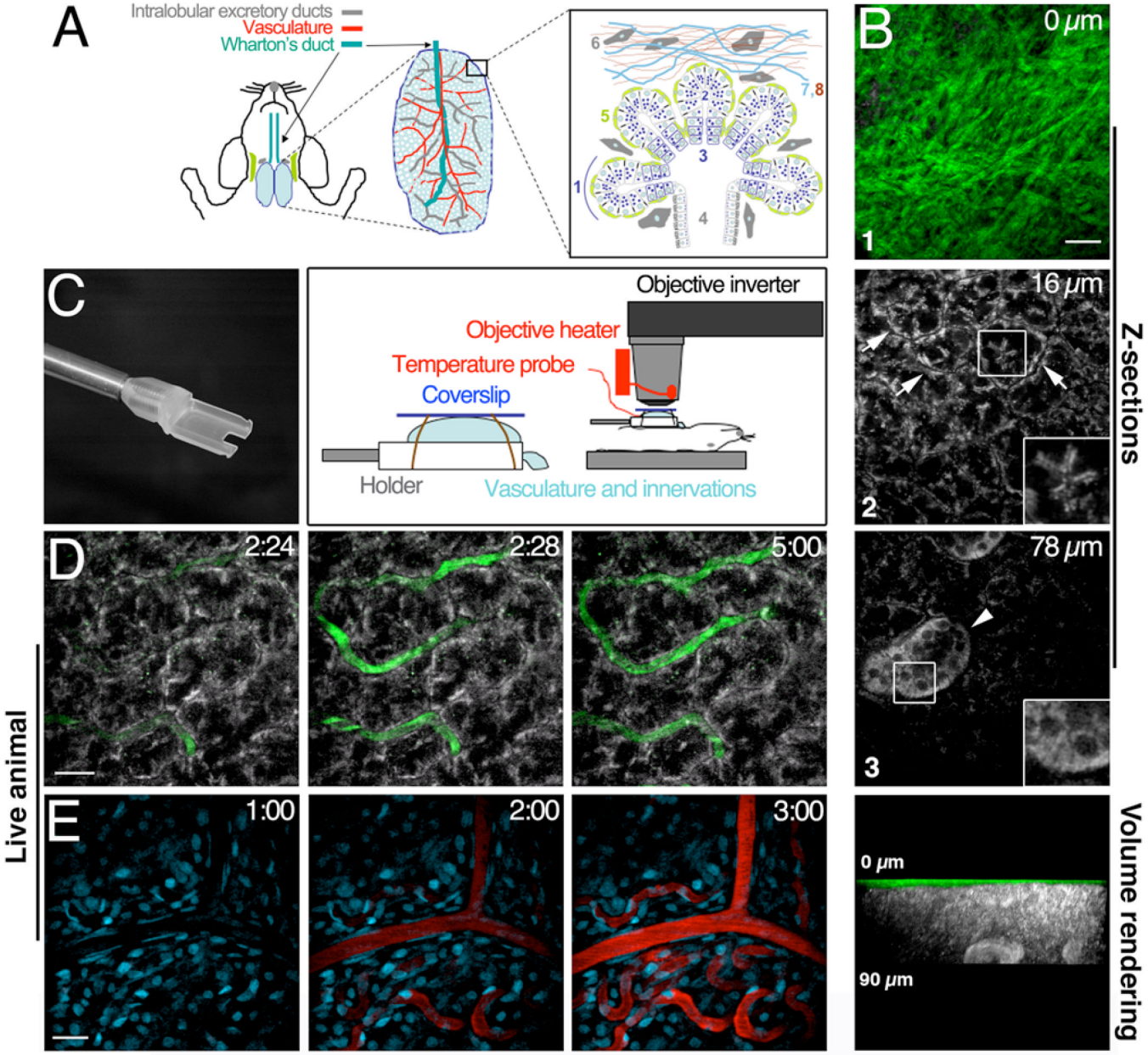

Figure 1. Characterization of the rat submandibular glands by TPM and SHG

A – Diagram of the rodent SSGs – The parenchyma of the SSGs is formed by acinar structures (1), which discharge secreted saliva into the acinar canaliculi (2). The contractions of the myoepithelial cells (5) facilitate the flow of the saliva first into the intercalated ducts (3) and later into the striated ducts (4), which join the interlobular ducts. The surface of the glands is covered by elastic fibers such as elastin (7) and collagen (8) and various populations of fibroblasts are scattered within the fibers and the parenchyma (6). **B** – Z-stacks and volume rendering of isolated rat SSGs - Z-stacks of the same area were acquired exciting first at 750 nm to image the parenchyma (grey) and then at 900 nm to image the elastic fibers (green). Acinar structures (arrows) and striated ducts (arrowhead) are also shown in the insets at a higher magnification. Lower panel - Side view of the volume rendering. **C** – Animal preparation – Left panel – Custom made holder designed for the SSGs. The notch has been designed to accommodate the vasculature, the Wharton's duct and the nerve terminals. Right panel –

Diagram showing the gland secured on the holder and covered with a glass coverslip. **D-E** - Dynamic imaging of the vasculature in rat SSGs –500 kDa FITC-D was injected in the tail artery of a rat (D) or a rat pre-injected with Hoechst 33342 (E) and imaged either at 750 nm to visualize the parenchyma of the glands (D, parenchyma grey, vasculature green) or at 800 nm to image the nuclei (E, nuclei cyan, vasculature red). Time of injection: 2'20" (D) and 1'32" (E). Bars 20 μm

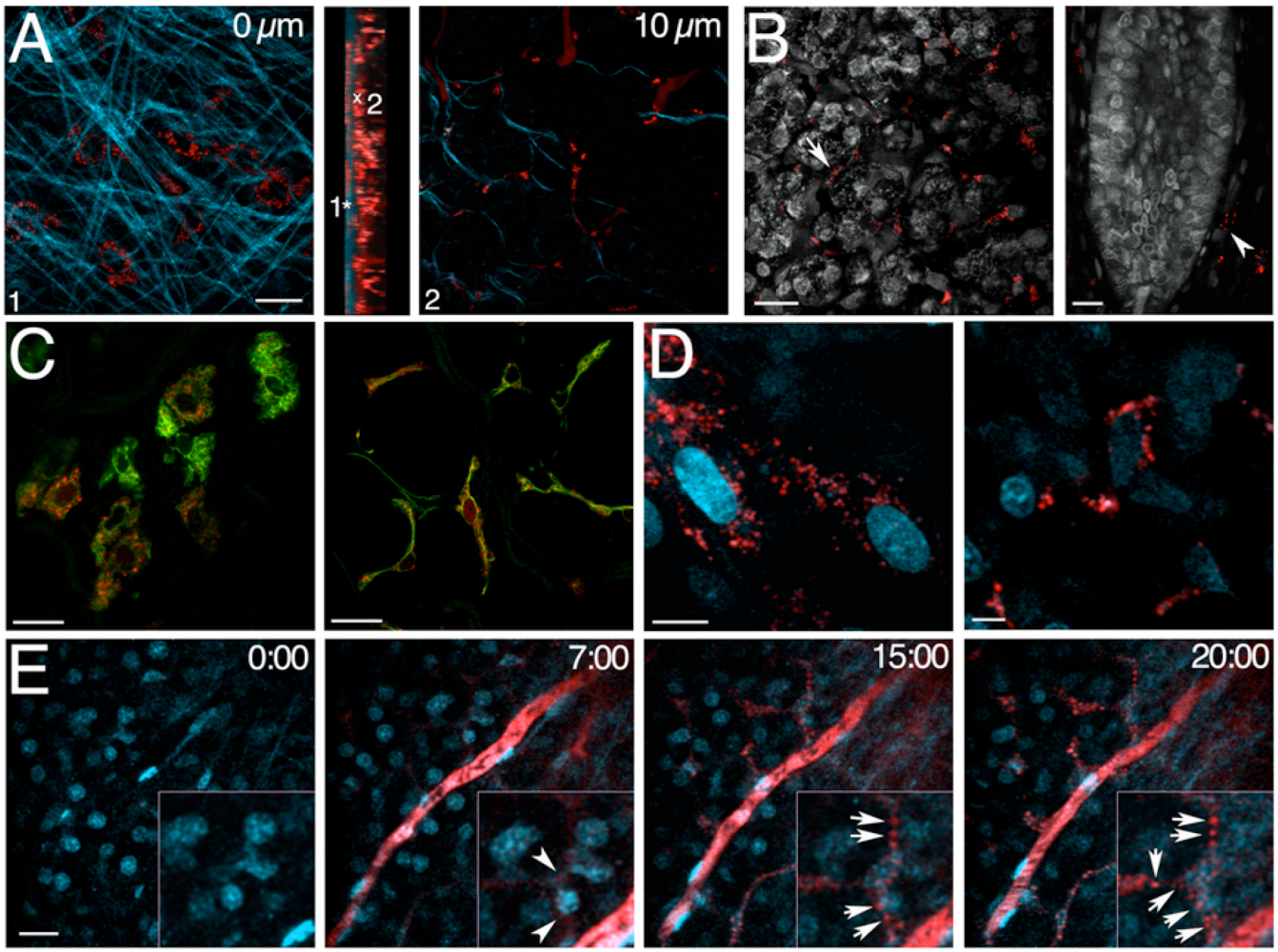

Figure 2. Fluorescent dextrans are internalized by fibroblasts in the SSGs of live rats

A-D - Rats were injected with TXR-D either alone (A,C) or in combination with 10 Hoechst 33343 (B,D) and the isolated glands were imaged immediately (A-B, D) or fixed and processed for immuno-staining (C). **A** - Isolated SSGs were imaged at different depth from the surface exciting at 830 nm to highlight the elastic fibers covering the gland (cyan) and the TXR-D (red). Center panel – Volume rendering (side view). TXR-D was internalized by cells lying at the surface of the gland (1) or in the stroma surrounding the acini (2). **B** - Intact (left panel) or longitudinally sectioned glands (right panel) were imaged at 750 nm to highlight the parenchyma. Arrow and arrowhead point to cells that internalized dextran around the acini and a large duct respectively.

C – SSGs were labeled with an antibody directed against vimentin (green) and imaged at the surface (left panel) or deeper into the gland (right panel) by confocal microscopy. **D** – High magnification of cells at the surface (left panel) or deeper into the gland (right panel) showing the sub-cellular distribution of internalized dextran. **E** - Time lapse imaging of dextran internalization in live animals - A rat was injected with Hoechst 33342, the SSGs were exposed and imaged at 830 nm (left panel – time -0:00). After 2 min and 30 sec, TXR-D was injected into the tail artery highlighting the vasculature almost instantly (see movie S5). After 4 min and 30 sec from the injection small round structures appeared inside cells adjacent to a blood vessel (time – 7:00, inset and arrowheads) which increased over time both in number (time -

15:00 min, inset and arrows) and in size (time - 20:00 inset and arrows). Bars in A,B,C and E 20 μm. Bar in D 10 μm.

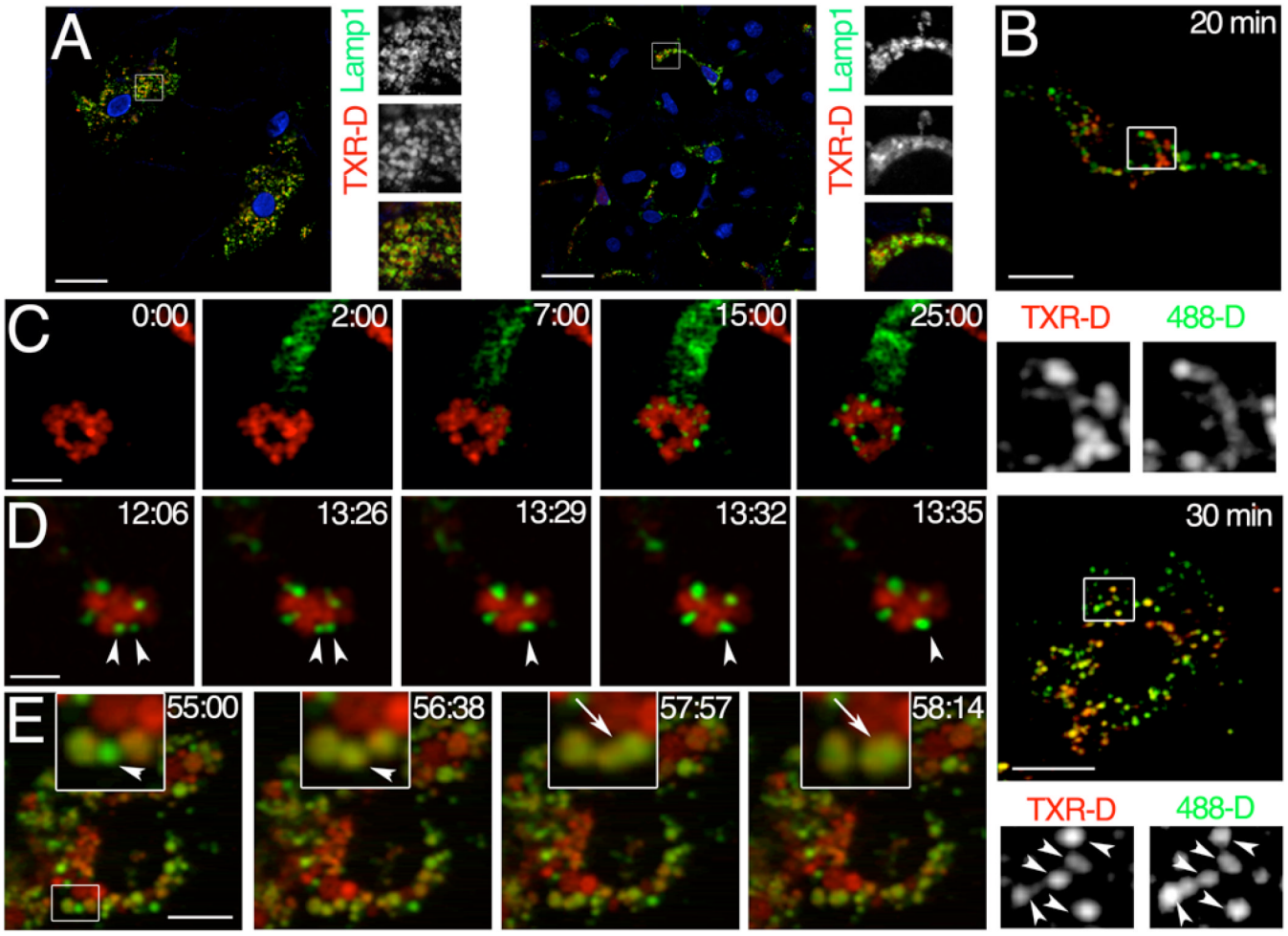

Figure 3. Trafficking of dextran from the early endosomes to the late/endosomes lysosomes

Rats were injected with TXR-D and after 24 hours either euthanized (A) or injected with 488-D (B-E). **A** – SSGs were isolated, fixed and labeled with an antibody directed against Lamp1 (green) and Hoechst 33342 (blue) Images were acquired by confocal microscopy. TXR-D is localized in structures decorated by Lamp1 (insets) both in cell located at the surface (left panels) and deeper in the tissue (right panels). Bars 20 μm. **B** – Twenty, and 30 minutes after the injection of the 488-D, the rats were euthanized, the glands were excised and imaged. At 30 minutes but not at 20 minutes a significant co-localization between 488-D and TXR-D was observed (insets, arrowheads). Bars 10 μm. **C-E** – Dynamic imaging of the trafficking of dextran through the endosomal compartments of live animals. - Before the injection of 488-D the glands were exposed and imaged at 830 nm. TXR-D containing lysosomes are shown in red - **C** – In the first 25 minutes after the internalization, endosomes grow in size but do not fuse with lysosomes. Bars 20 μm. **D** - Small early endosomes undergo fusion (arrowheads). Bars 20 μm. **E** – After 55 min from the injection we observed a 488-D containing endosomes (time 55:00, inset arrowhead), which acquired first TXR-D (time 56:38, inset and arrowhead) and then fused with a structure containing both 488-D and TXRD (time 57:57 and 58:14, insets and arrows). Bars 10 μm.

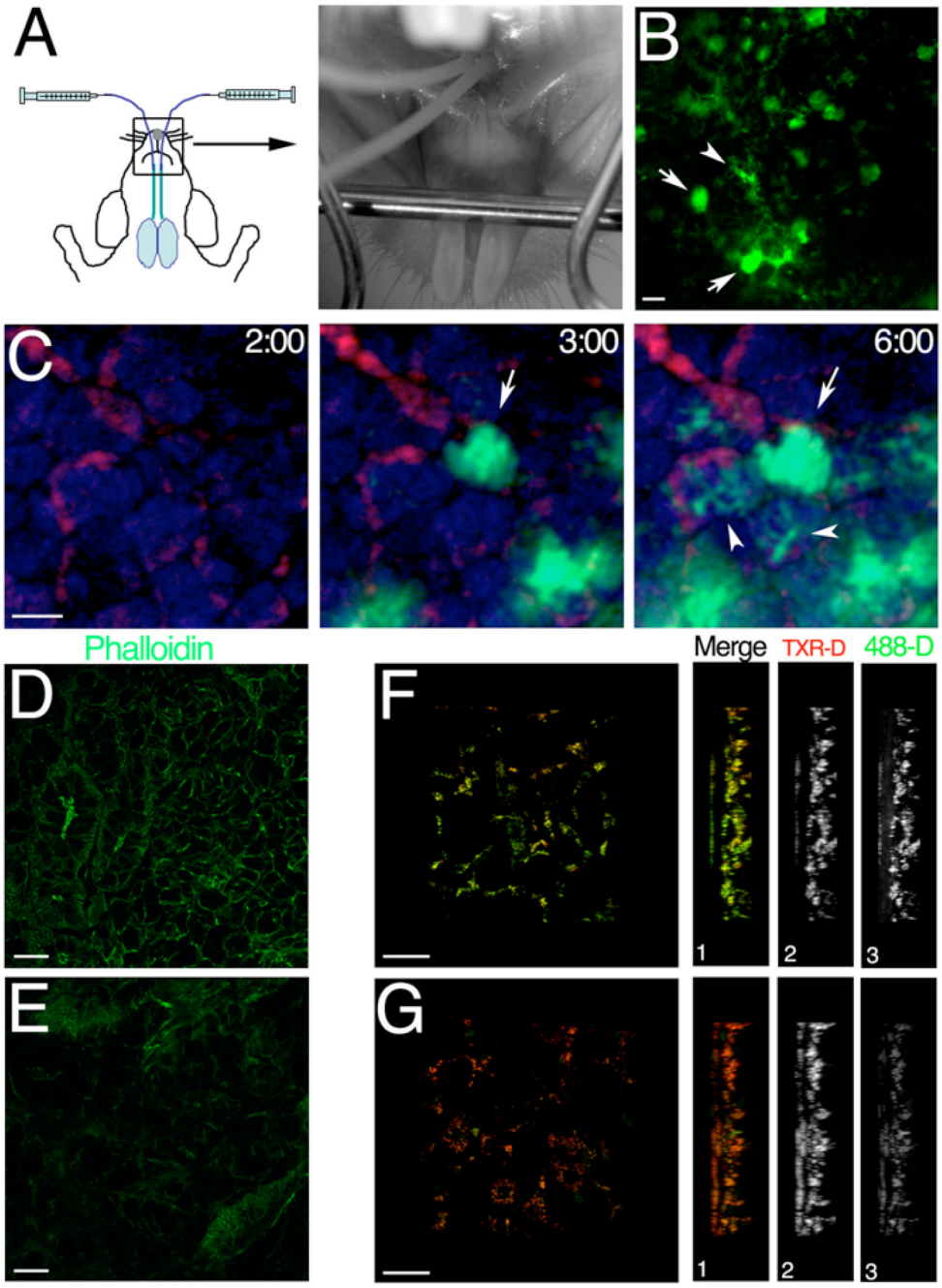

Figure 4. Delivery of molecules to the rat SSGs through the Wharton's duct

A – Cannulation of the Wharton's duct – The rats were placed onto an adjustable stage and two thin cannulae were inserted into the Wharton's ducts from the orifices below the tongue (right panel, arrowhead) - **B-C** – Injection of 488-D into the Wharton's duct - 20 μg of 488-D were injected through the cannula into the Wharton's duct either alone (B) or in combination with 200 μg of systemically injected TXR-D (C). B – Snapshot showing the SSGs after 5 minutes after injection of 488-D. Arrows point to the cross section of large ducts, while the arrowhead points to a series of smaller ducts. - C - The SSG was exposed and imaged at 750 nm to highlight the parenchyma of the SSGs. The vasculature is shown in red. 488-D (green) appeared first in large ducts (arrows), and later in smaller ducts and acini canaliculi

(arrowheads). **D-G** – Effect of LatA and CytD on the SSGs. TXR-D was systemically injected in a rat. After 1hr two cannulae were inserted in the Wharton's ducts and one of the glands was injected with 10 μM LatA while the other was injected with the vehicle (control). After 45 minutes the rat received a systemic injection of 488-D and 1 hour later the animal was euthanized. First, the glands were imaged at 830 nm (F-G) and then frozen and processed for cryo-sections and immunolabeling (D-E). D, E – Both glands were sectioned, labeled with Alexa 488-phalloidin and imaged by confocal microscopy. F,G – 3D reconstructions of the first 60 μm below the surface of the glands. The levels of TXR-D (red), that was injected before Lat A, were not affected, while the amount of internalized 488-D (green) was substantially reduced (side view). Bars 20 μm